DIRECT NUMERICAL SIMULATION OF TRANSITION IN COMPRESSIBLE FLOWS

N. A. Adams
ETH Zürich, Institute of Fluid Dynamics,
ETH Zentrum, CH-8092 Zürich, Switzerland
Nikolaus.Adams@ethz.ch

Abstract In this paper we present first results on the transition of the separated boundary layer along a compression ramp at Mach 5 as an example for today's capabilities of direct numerical simulation of transition in complex shear flows. The computational method is based on the 5th order hybrid compact-ENO method of Adams and Shariff, 1996. The flow parameters of the considered configuration are adjusted to an experimentally feasible configuration. The shock-induced laminar separation extends for about 20 incoming-boundary-layer thicknesses. We find that for the two-dimensional solution following a two-dimensional second mode instability imposed at inflow the unsteady fluctuations with respect to the mean remain small upto rather large excitation levels of the inflow disturbance. No indications for a global instability of the two-dimensional steady solution have been found so far. Even at large inflow-disturbance excitation levels the two-dimensional flow exhibits a split into a nearly steady solenoidal part and an unsteady acoustic part. If in addition to the second mode an unstable first oblique mode is imposed at inflow, streamwise vortices are generated in the detached shear layer.

1. Introduction

An example for the importance of transition in aerodynamic configurations is the effectiveness of control surfaces of re-entry vehicles whose flight corridor passes through a regime of comparably low Reynolds number (Muylaert and Berry, 1998; Berry et al., 1999). Also, down-sized experimental vehicles or rescue vehicles can exhibit laminar or transitional flows along most of their body surface during re-entry since at supersonic and hypersonic speed transition is delayed. For incompressible boundary layers transition mechanisms are fairly well understood (Kleiser and Zang, 1991; Kachanov, 1994). Transition in compressible boundary-

layers was subject of intense investigations in the recent past (Thumm et al., 1990; Pruett and Zang, 1992; Pruett et al., 1995; Pruett and Chang, 1995; Pruett and Chang, 1998; Eißler and Bestek, 1996; Adams and Kleiser, 1996; Mielke, 1999; Mielke and Kleiser, 1999, e.g.). To our knowledge only very few initial studies have been performed so far on transition in supersonic boundary layers with shock-boundary-layer interaction (Pagella et al., 2000; Lawal and Sandham, 2001). Linearized theories for compressible turbulence (Kovasznay, 1953) and shock-turbulence interaction (Ribner, 1953; Ribner, 1954) were early theoretical developments. From these it is known that the interaction with a shock-wave couples the otherwise independent linear modes (vorticity mode, acoustic mode, entropy mode).

The laminar base flow along a supersonic compression ramp with sufficiently large deflection exhibits an area of separated flow which is considerably larger than that for turbulent flow (Adamson and Messiter, 1980). Simplified linear stability analysis such as for zero-pressure gradient boundary layers cannot be performed for the compression ramp flow. The dominant transition mechanisms for this configuration are unknown. For separated flows a global eigenmode analysis was proposed by Theofilis et al., 2000.

With the numerical study, for which we present first results in this paper, we assume that transition takes place in a low-noise environment. We expect that receptivity near the leading edge initiates a "natural" transition through the most unstable linear eigenmodes of the laminar attached boundary layer. The flow parameters of our setup are adjusted to that of a planned experiment (see section 2) which is a generic model for the flow encountered near the body flap of a re-entry vehicle. For a flat-plate boundary-layer at high free-stream Mach numbers two instability modes of different character coexist, the first-mode instability which is of vorticity character, and the second-mode (or Mack-mode) instability which is of mixed vorticity-acoustic type (Mack, 1984; Mack, 1990). Whereas the former is oblique, i.e. it travels downstream at an angle with respect to the freestream, the dominant second mode instability is two-dimensional. The relevance of the second mode for laminar-turbulent breakdown is unclear at present (Stetson and Kimmel, 1992; Pruett and Chang, 1998, e.g.). It is known that these two types of instabilities behave differently with respect to boundary-layer non-parallelity (El-Hady, 1991) and wall-heating (Mack, 1984).

A two-dimensional second mode instability cannot initiate transition without a secondary instability mechanism which most likely follows a subharmonic or H-type route (Pruett and Zang, 1992; Adams and Kleiser, 1996). For the first mode a secondary instability mechanism is

Parameter	Value	Comment
M_∞	5	
Re_{δ_0}	5967	at inflow
Re_{δ_1}	4319	at inflow
δ_1^*	$6.84 \cdot 10^{-4}$	$[m]$, at inflow
T_∞^*	83.33	$[K]$
T_W	$4.8\ T_\infty^*$	
S^*	$110.4K$	
U_∞^*	915	$[m/s]$
p_∞^*	945	$[Pa]$

Table 1. Flow parameters.

not required (Thumm et al., 1990; Adams and Kleiser, 1993). Since prior to reattachment the mean streamlines are curved, also a Görtler instability can exist.

2. Problem formulation

We adapt the flow parameters to an experimental setup proposed in a preliminary version of the Stage I Report of the RTO Working Group 10 on "Technologies for Propelled Hypersonic Flight", Subgroup 3 "CFD Validation for Hypersonic Flight", Version January 7, 2000, data set number 2, heated hollow cylinder flare, by B. Chanetz and J, P, Davis. In the final version of this report (Knight, 2000) this proposed experimental data set unfortunately has been discarded. It appears, however, to be a suitable candidate for DNS. The flow parameters are given in table 1, quantities with a star superscript are dimensional, other quantities are non-dimensionalized by the displacement thickness at inflow δ_1 and free-stream quantities. The situation of the computational domain with respect to the experiment is indicated in figure 1(a), the corresponding geometrical parameters are given in table 2. The computational domain is indicated by a solid frame, the experimental-model contours are indicated by a dashed line. Whereas the experimental model is a hollow-cylinder flare combination we neglect the spanwise curvature and use a plane compression ramp as computational representation. To avoid the leading-edge singularity the computational domain starts at a distance x_0^* downstream of the leading edge. We set the wall temperature equal to the adiabatic-wall temperature of the incoming laminar boundary layer. The incoming boundary layer profiles are taken from a similarity solution, figure 2.

To achieve consistency with the free-stream conditions, the wall-normal component $w(z)$ of the similarity solution is ramped exponentially to

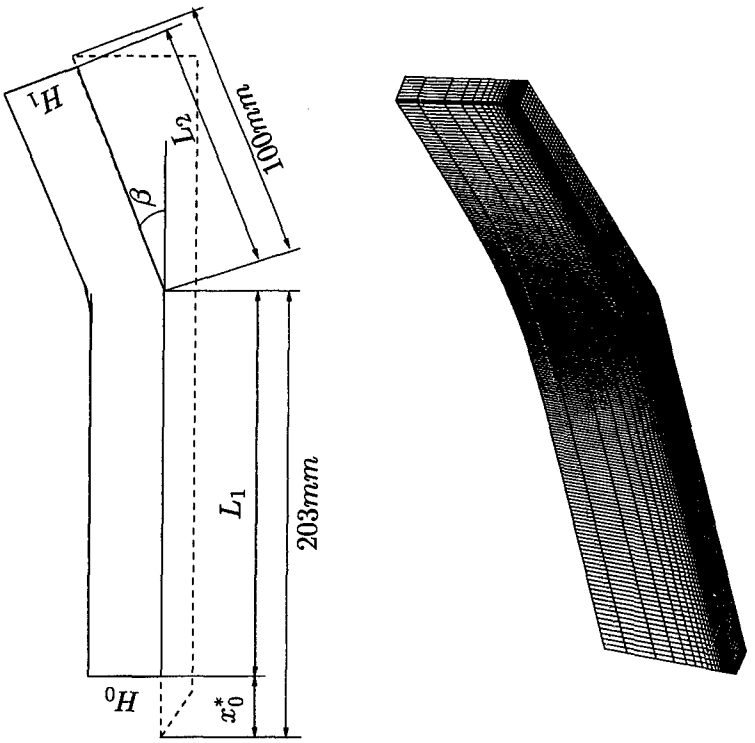

(a) Sketch of the setup, ——— computational domain, - - - - model contour.

(b) Computational mesh, not every grid is line shown.

Figure 1. Compression ramp configuration.

Parameter	Value	Comment
x_0^*	$2.53 \cdot 10^{-2}$	$[m]$, distance from l.e.
L_1	260	
L_2	147	
β	15°	
H_0	60	
H_1	60	
L_x	357	
L_y	12.6	

Table 2. Geometric parameters.

Parameter	First mode	Second mode
α_r	0.4828	2.2061
α_i	−0.0064	−0.0123
β	1	0
ω	0.4	2

Table 3. Eigenvalues of first and second mode instability.

zero outside of the boundary layer. For the similarity solution we perform a spatial linear stability analysis assuming parallel flow. We pick a second mode near its maximum spatial growth rate with the eigenvalues given in table 3. The amplitude distribution of the second mode is shown in figure 3(a). The phase velocity of the second mode is $c_{Phase} = 0.91$ so that the mode travels with almost the free-stream velocity. It is of vorticity character above the relative sonic layer and of acoustic character below (Mack, 1990). An unstable first mode is given

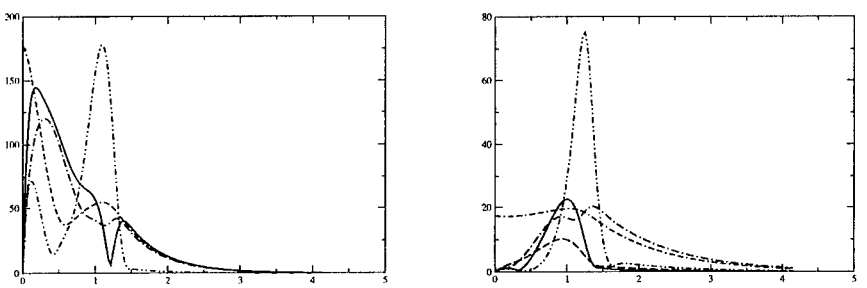

(a) Second mode: ——— $10 \cdot u'(z)$, —·— $10 \cdot w'(z)$, ·--· $\rho'(z)$, ——··—— $100 \cdot p'(z)$.

(b) First mode: ——— $u'(z)$, , —·— $10 \cdot w'(z)$, ·--· $\rho'(z)$, ——··—— $100 \cdot p'(z)$.

Figure 3. Amplitude distributions.

by the parameters in table 3, where the frequency was chosen to be an integer fraction of the second mode frequency. The amplitude distribution of the first mode is shown in figure 3(b). The first mode travels downstream with a phase velocity of $c_{Phase} = 0.83$. Near the critical layer z_{cr}, where $u(z_{cr}) = c_{Phase}$, the density fluctuations have maximum amplitude.

The fundamental equations solved are the conservation equations for mass, momentum and energy in generalized coordinates

$$\frac{\partial}{\partial t}\frac{U}{J} + \frac{\partial}{\partial \xi}\frac{F_E}{J} + \frac{\partial}{\partial y}\frac{G_E}{J} + \frac{\partial}{\partial \zeta}\frac{H_E}{J} = \frac{\partial}{\partial \xi}\frac{F_S}{J} + \frac{\partial}{\partial y}\frac{G_S}{J} + \frac{\partial}{\partial \zeta}\frac{H_S}{J} \quad ,$$

where the conservative variables are $U = \{\rho,\ \rho u,\ \rho v,\ \rho w,\ E\}$, with $E = p/(\gamma - 1) + \rho(u^2 + v^2 + w^2)/2$. Considering only essentially two-dimensional configurations we limit the coordinate generalization to the (x, z)-plane. The physical space (x, y, z) is mapped onto the computational space (ξ, η, ζ) which is Cartesian and equi-spaced. The convective and diffusive fluxes are detailed in Adams, 1998.

At the inflow all dependent variables are imposed. At the no-slip wall all velocities are set to zero and the wall temperature is prescribed. At the outer truncation plane Dirichlet boundary conditions fixing all variables at their free-stream values are imposed. At the outflow plane inviscid non-reflecting boundary conditions of Thompson, 1987, are applied.

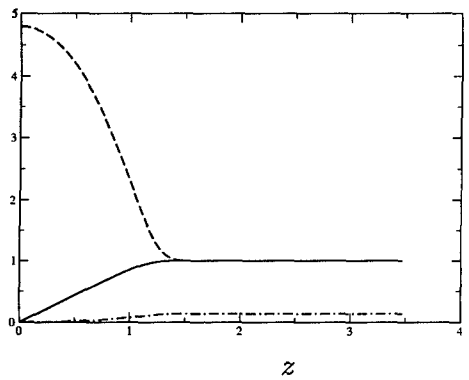

Figure 2. Similarity solution for the incoming boundary layer: ——$u(z)$, - - - -$T(z)$, —·—$10 \cdot w(z)$.

The mapping of the rectangular, evenly spaced computational mesh onto the physical mesh as shown in figure 1(b) is outlined in Adams, 1998. The mapping parameters are adjusted so that about half of the wall-normal grid points are located at $z \leq 6$. Grid points are condensed in streamwise direction towards the corner. The corner itself is smoothed so that it can be resolved on the mesh, curvature radius at the corner is 0.5, whereas the curvature radius of the upper truncation plane is 50.

A family of symmetric compact finite difference schemes with spectral-like resolution has been introduced by Lele, 1992. They are being widely used for direct numerical simulation of transitional and turbulent shear flows (Adams and Kleiser, 1996; Pruett et al., 1995, e.g.) and aeroacoustic problems. As with spectral schemes symmetric compact schemes are sensitive to boundary condition formulation and aliasing errors. The latter is of particular concern for the discretization of convective terms

in the Euler or Navier-Stokes equations, where triple products appear in the conservative form of the momentum equations.

In this study we use compact upwind schemes for the discretization of convection terms, a class of which has been derived from a generalized formulation of compact schemes by Adams and Shariff, 1996, and Adams, 1998. The schemes have a centered stencil but become upwind biased due to non-symmetric coefficients. The upwind biasing introduces a certain amount of numerical dissipation at non-resolved wave numbers which allows to contain aliasing errors. At discontinuities, the scheme is coupled to a high-order essentially non-oscillatory scheme (Shu and Osher, 1989) as described in Adams and Shariff, 1996, and in Adams, 1998.

DNS codes are required to resolve all scales appearing in a flow problem. For that reason it is necessary to perform two different kind of tests, the first of which is to assess how well fluctuations about a mean flow are represented, the second is to see how well the mean flow itself can be computed. Concerning the first, results from linear stability theory can be used as a reference. For the second, comparison with steady-state computations and experimental results for laminar compression ramp flow should be sufficient, in this case the ENO-scheme is active around the shock. These tests have been successfully applied to the the present numerical method. The results are documented in Adams, 1998.

3. Simulation results

The analysis of transition in shear flows requires to accurately establish the steady base flow first. Although for compression-corner flows with separation it is not clear *a priori* that a steady two-dimensional solution exists, such a solution was found for our flow configuration. Since all computations were performed with explicit time integration without convergence acceleration, the steady-state computations were rather time consuming. After the steady-state solution was established, two-dimensional inflow disturbances were created by superimposing a second Mack mode at a sufficiently large amplitude, resulting in an unsteady two-dimensional flow. The separate analysis of this two-dimensional solution which cannot exhibit laminar-turbulent break down, is helpful to distinguish the effects of the two-dimensional Mack mode from the three-dimensional setting where both first and second mode instabilities are active. Eventually, the two-dimensional steady solution is perturbed by superimposing a combination of first and second mode instability.

Set	N_x	N_z
2D	400	100
2DF	1000	140
2DFF	1500	180
2DFFF	2000	240

Table 4. Mesh resolution for different data sets of the steady flow solution.

3.1 Steady flow

As initial data we use a laminar flat plate boundary layer similarity solution along the ramp surface, developing as if there was no streamwise pressure gradient. In the exterior of the boundary layer an inviscid Euler solution for the compression-ramp flow is imposed. The initial evolution is computed by a 3rd order ENO scheme with a Roe flux formulation with entropy fix (Shu and Osher, 1989), which is more dissipative than the CUVB scheme used eventually for the later stages (Adams and Shariff, 1996; Adams, 1998). In figure 4 we show the evolution of the skin friction coefficient and the wall pressure from the initial distribution. For each of the resolutions given in table 4 the corresponding steady state solution is shown. It is obvious that the length of the laminar separation depends strongly on the numerical diffusion introduced by the discretization and on the mesh resolution. With the last refinement levels 2DFF and 2DFFF an almost mesh independent solution is achieved.

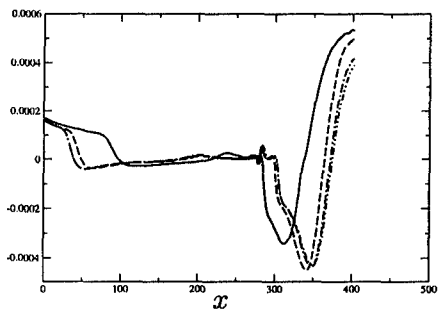

(a) C_f with increasing mesh resolution, ——set 2D, – – – –set 2DF, —·—set 2DFF, —··—set 2DFFF.

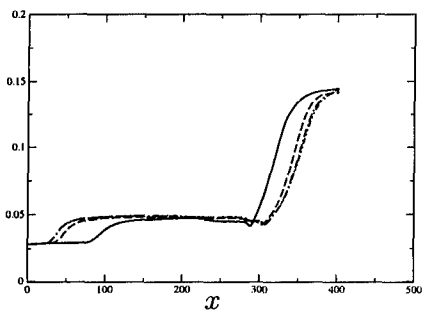

(b) p_W with increasing mesh resolution, ——set 2D, – – – –set 2DF, —·—set 2DFF, —··—set 2DFFF.

Figure 4. Evolution of the steady-state skin friction coefficient and the wall pressure.

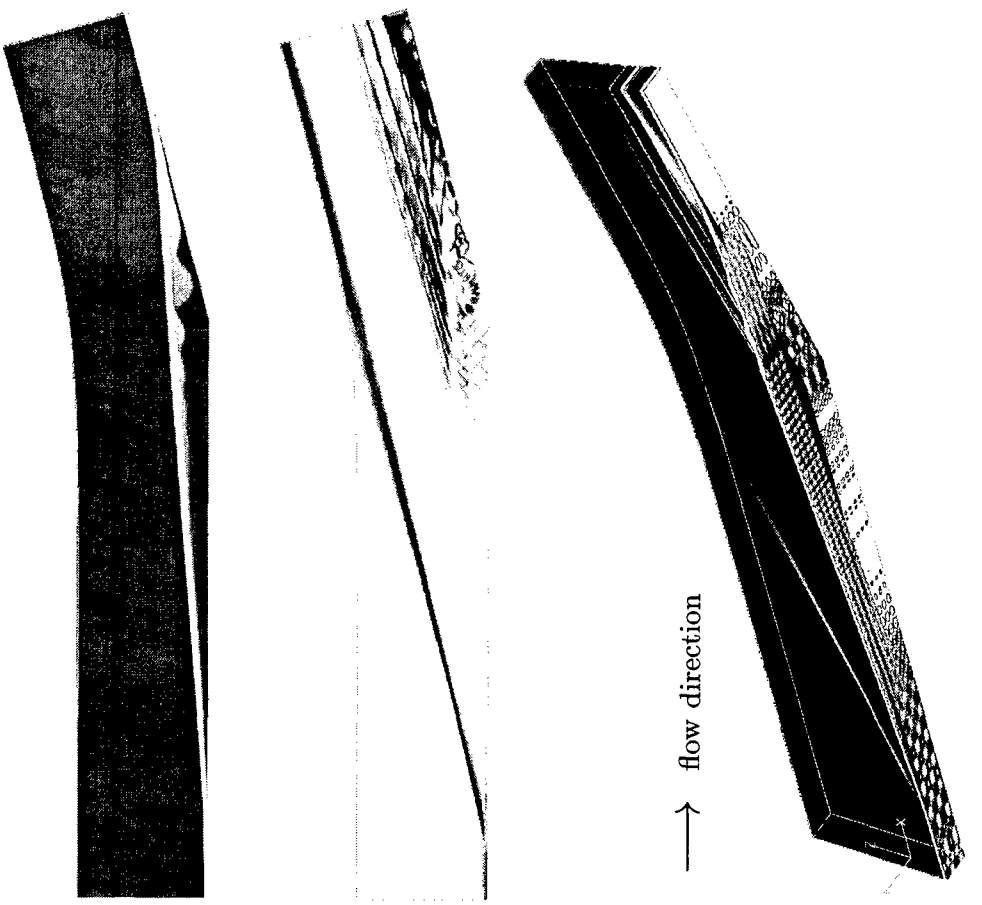

(a) ω_y, grey scales from light -0.2 to dark 0.2.

(b) $|\nabla p|$, grey scales from dark 0 to light 0.003.

(c) Iso-surface of $|\omega_x| = 4.7 \cdot 10^{-4}$: grey shaded, $|\nabla \rho|$ in the computational planes $\eta = 1$, $\xi = 1$: grey coded between 0 and 0.2, contours of $|\omega_x|$ in the plane $\zeta = 0$: grey coded between 0 and $1 \cdot 10^{-4}$.

Figure 5. Steady spanwise-vorticity distribution (a), instantaneous pressure-gradient magnitude (b), and instantaneous visualization at time $t = 372$ after imposing the inflow perturbation (c).

3.2 Two-dimensional unsteady flow

For the unsteady two-dimensional solution we have further increased the spatial resolution to $N_x = 5000$ and $N_z = 320$ cells, for which the

solution can be considered as converged. A reasonable estimate for the amplitude reached by the most unstable linear eigenmodes at inflow is $\max(u')/U_\infty \simeq 10^{-4}$. Given the streamwise growth rates, this is the amplitude roughly reached by the most unstable eigenmodes growing from low-level noise near the leading edge. Since the maximum amplitude of the density eigenfunction is about one order of magnitude larger than that of the streamwise velocity eigenfunction for both first and second mode, one can expect that at a larger amplitude linear theory is no longer a good approximation. We found, however, that imposing the second mode instability scaled with $\max(u')/U_\infty \simeq 10^{-4}$ had no visible effect on the solution. The imposed second mode instability in fact turned out to be stable in the attached part of the spatially growing boundary layer. This behavior is consistent with the finding of El-Hady, 1991, that boundary-layer non-parallelity stabilizes a two-dimensional second mode, compared with the result for parallel flow. The second mode instability neither was able to trigger an instability in the detached shear layer. Only at a significantly increased amplitude of $\max(u')/U_\infty = 0.05$ the flow unsteadiness became significant with considerable excursions of skin friction and surface pressure from the mean. It is found that the instability creates mainly acoustic waves traveling downstream while being reflected back and forth between the detached shear layer and the wall. The solenoidal flow structure remains almost steady. An instantaneous ω_y distribution is almost indistinguishable from the steady state solution in figure 5(a). The acoustic component, however, is highly unsteady, as a snapshot of pressure-waves indicates shown in figure 5(c).

3.3 Three-dimensional unsteady flow

Since in three-dimensions a similarly fine resolution as in the two-dimensional unsteady case is unaffordable, we have chosen the streamwise resolution as $N_x = 3000$ and the wall-normal resolution as $N_z = 180$. This leaves room for a spanwise-domain size of two first-mode spanwise wavelengths, discretized with $N_y = 90$ points. In this case we can consider the resolution being somewhat finer than case 2DFF of section 3.1 as sufficient, albeit not fully mesh independent. The three-dimensional simulations are in progress and we can only show preliminary instantaneous results in this paper. The final results will be published elsewhere. For the present results at time $t = 372$ after imposing the inflow perturbation, the inflow disturbance has not yet reached the outflow plane. The instantaneous skin friction coefficient C_f and the instantaneous surface pressure show only a weak unsteadiness near the corner and near boundary-layer reattachment. An snapshot of the flow

at $t = 372$ shows the generation of streamwise vortices from the first mode instability in the detached shear layer, figure 5(c).

4. Concluding remarks

This paper presents first results of an ongoing research project, final results will be presented elsewhere. The author acknowledges the Swiss Center for Scientific Computing for providing CPU time on its NEC SX-5 computer.

References

Adams, N. A. (1998). Direct numerical simulation of turbulent compression corner flow. *Theor. Comp. Fluid Dyn.*, 12:109–129.

Adams, N. A. and Kleiser, L. (1993). Numerical Simulation of Fundamental Breakdown of a Laminar. *AIAA Journal*, 93-5027.

Adams, N. A. and Kleiser, L. (1996). Subharmonic transition to turbulence in a flat plate boundary layer at Mach number 4.5. *J. Fluid Mech.*, 317:301–335.

Adams, N. A. and Shariff, K. (1996). A high-resolution hybrid compact-ENO scheme for shock-turbulence interaction problems. *J. Comp. Phys.*, 127:27–51.

Adamson, T. C. and Messiter, A. F. (1980). Analysis of two-dimensional interactions between shock waves and boundary layers. *Annu. Rev. Fluid Mech.*, 12:103–138.

Berry, S. A., T. J. Horvath, B. R. H., Thompson, R. A., and H. H. Hamilton II (1999). X-33 hypersonic boundary layer transition. *AIAA-paper*, 99-3560.

Eißler, W. and Bestek, H. (1996). Spatial Numerical Simulation of Linear and Weakly Nonlinear Instabilities in Supersonic Boundary Layers. *Theoret. Comput. Fluid Dynamics*, 8:219–235.

El-Hady, N. M. (1991). Nonparallel instability of supersonic and hypersonic boundary layers. *Phys. Fluids*, A 3(9):2164–2178.

Kachanov, Y. (1994). Physical Mechanisms of Laminar-Boundary-Layer Transition. *Annu. Rev. Fluid Mech.*, 26:411–482.

Kleiser, L. and Zang, T. (1991). Numerical Simulation of Transition in Wall-Bounded Shear Flows. *Annu. Rev. Fluid Mech.*, 23:495–537.

Knight, D. (2000). RTO Working Group 10, "Technologies for Propelled Hypersonic Flight", Subgroup 3, "CFD Validation for Hypersonic Flight", Stage I Report. http://coewww.rutgers.edu/~wg10/report.pdf.

Kovasznay, L. S. G. (1953). Turbulence in supersonic flow. *J. Aero. Sci.*, 20:657–682.

Lawal, A. A. and Sandham, N. D. (2001). Direct simulation of transonic flow over a bump. In Geurts, B. J., Friedrich, R., and Metais, O., editors, *Direct and Large-Eddy Simulation IV*. Kluwer Academic Publishers.

Lele, S. K. (1992). Compact finite difference schemes with spectral-like resolution. *J. Comp. Phys.*, 103:16–42.

Mack, L. (1984). Boundary-Layer Linear Stability Theory. *AGARD Report No. 709*, pages 3-1 to 3-81.

Mack, L. (1990). On the inviscid acoustic-mode instability of supersonic shear flows. Part I: Two-dimensional waves. *Theor. Comput. Fluid Dyn.*, 2:97–123.

Mielke, C. (1999). *Numerische Untersuchungen zur Turbulenzentstehung in dreidimensionalen kompressiblen Grenzschichtströmungen.* PhD thesis, ETH Zürich, Diss. Nr. 13344.

Mielke, C. and Kleiser, L. (1999). Investigation of transition to turbulence in a 3D supersonic boundary layer. In *Proceedings of the IUTAM Symposium on Laminar–Turbulent Transition.*

Muylaert, J. and Berry, W. (1998). Aerothermodynamics for space vehicles - ESA's activities and the challenges. *ESA bulletin*, 96.

Pagella, A., Rist, U., and Wagner, S. (2000). Numerical investigations of small-amplitude disturbances in a laminar boundary layer with impinging shock waves. In *Proceedings of the 12. DGLR Fach-Symposium AG Stab.*

Pruett, C. D. and Chang, C.-L. (1995). Spatial direct·numerical simulation of high-speed boundary layer flows – part II: transition on a cone in Mach 8 flow. *Theor. Comp. Fluid Dyn.*, 7:397–424.

Pruett, C. D. and Chang, C.-L. (1998). Direct numerical simulation of Hypersonic boundary–layer flow on a flared cone. *Theoret. Comput. Fluid Dynamics*, 11:49–67.

Pruett, C. D. and Zang, T. (1992). Direct numerical simulation of laminar breakdown in high-speed, axisymmetric boundary layers. *Theor. Comp. Fluid Dyn.*, 3:345–367.

Pruett, C. D., Zang, T., Chang, C.-L., and Carpenter, M. H. (1995). Spatial direct numerical simulation of high-speed boundary-layer flows – part I: algorithmic considerations and validation. *Theor. Comp. Fluid Dyn.*, 7:49–76.

Ribner, H. S. (1953). Convection of a pattern of vorticity through a shock wave. Technical Report TN 2864, NACA.

Ribner, H. S. (1954). Shock-turbulence interaction and the generation of noise. Technical Report TN 3255, NACA.

Shu, C.-W. and Osher, S. (1989). Efficient implementation of essentially non-oscillatory shock-capturing schemes, II. *J. Comput. Phys.*, 83:32–78.

Stetson, K. and Kimmel, R. (1992). On Hypersonic Boundary-Layer Stability. *AIAA Paper*, 92-0737.

Theofilis, V., Hein, S., and Dallmann, U. (2000). On the origins of unsteadiness and three-dimensionality in a laminar separation bubble. *Phil. Trans. R. Soc. Lond. A*, 358:3229–3246.

Thompson, K. W. (1987). Time dependent boundary conditions for hyperbolic systems. *J. Comput. Phys.*, 68:1–24.

Thumm, A., Wolz, W., and Fasel, H. (1990). Numerical simulation of spatially growing three–dimensional disturbance waves in compressible boundary layers. In Arnal, D. and Michel, R., editors, *Laminar–Turbulent Transition IUTAM Symposium Toulouse, France, 1989*, pages 303–308. Springer Verlag.